A novel layered topology of auxetic materials based on the tetrachiral honeycomb microstructure

Ferdinando Auricchio [a], Andrea Bacigalupo [b,*], Luigi Gambarotta [c], Marco Lepidi [c], Simone Morganti [d], Francesca Vadalà [c]

[a] Department of Civil Engineering and Architecture, University of Pavia, Italy
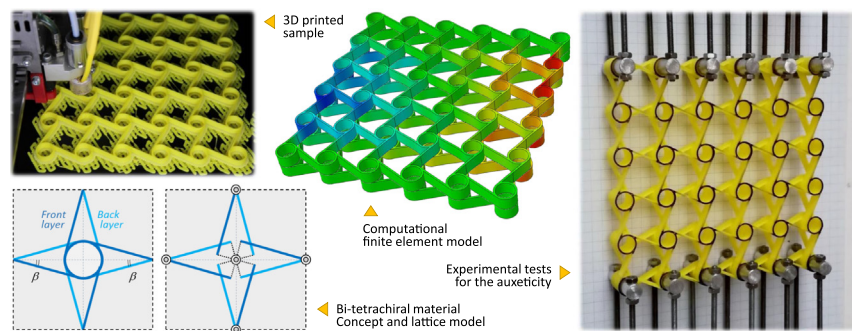[b] IMT School for Advanced Studies Lucca, Italy
[c] Department of Civil, Chemical and Environmental Engineering, University of Genova, Italy
[d] Department of Electrical, Computer, and Biomedical Engineering, University of Pavia, Italy

HIGHLIGHTS

- A novel layered topology of auxetic cellular materials based on the tetrachiral honeycomb microstructure, named *bi-tetrachiral* material, is proposed.
- The global elastic properties of 3D printed samples of the bi-tetrachiral material are experimentally identified from quasi-static tensile tests.
- Computational finite element models and beam lattice models efficiently reproduce the experimental response of the bi-tetrachiral material.
- The mutual collaboration of two tetrachiral layers with opposite chirality prevents the development of global angular strains under tensile loads.
- Parametric analyses show that Poisson ratios close to −1 are achievable by regulating the distance between the inter-layer constraints.

GRAPHICAL ABSTRACT

ARTICLE INFO

ABSTRACT

Microstructured honeycomb materials may exhibit exotic, extreme and tailorable mechanical properties, suited for innovative technological applications in a variety of modern engineering fields. The paper is focused on analysing the directional auxeticity of tetrachiral materials, through analytical, numerical and experimental methods. Theoretical predictions about the global elastic properties have been successfully validated by performing tensile laboratory tests on tetrachiral samples, realized with high precision 3D printing technologies. Inspired by the kinematic behaviour of the tetrachiral material, a newly-design bi-layered topology, referred to as bi-tetrachiral material, has been theoretically conceived and mechanically modelled. The novel topology virtuously exploits the mutual collaboration between two tetrachiral layers with opposite chiralities. The bi-tetrachiral material has been verified to outperform the tetrachiral material in terms of global Young modulus and, as major achievement, to exhibit a remarkable auxetic behaviour. Specifically, experimental results, confirmed by parametric analytical and computational analyses, have highlighted the effective possibility to attain strongly negative Poisson ratios, identified as a peculiar global elastic property of the novel bi-layered topology.

* Corresponding author.
  E-mail address: andrea.bacigalupo@imtlucca.it (A. Bacigalupo).

1. Introduction

Architectured composite materials characterized by a cellular honeycomb microstructure are experiencing an increasing success in a variety of innovative technological applications, by virtue of superior and tailorable physical-mechanical properties [1–3]. Among the other cellular topologies, honeycomb materials based on chiral and anti-chiral microstructures can offer peculiar extreme features of directional auxeticity, frequently conjugated with functional performance of high resistance to fracture and indentation, atypical bending with synclastic curvatures, enhanced strength against buckling instabilities [4–12]. Furthermore, the fine parametric tunability of the microstructural inertia and stiffness allows the systematic employment of chiral and anti-chiral materials to realize efficient and versatile phononic filters, elastic waveguides and acoustic diodes [13–18]. Within this challenging framework, the optimal design of the micromechanical properties opens interesting research perspectives towards the theoretical conceptualization and experimental validation of a new generation of smart materials targeted at innovative engineering applications, including impact absorption, negative refraction, shape morphing, wave trapping, vibration shielding, noise silencing and invisibility cloaking [19–22].

Focusing the attention on the modern scientific literature about quasi-static laboratory tests of architectured materials, a pioneering investigation has experimentally verified the theoretical possibility to achieve strong auxetic properties (quantified by negative Poisson ratios close to unity) in medium-size samples of planar hexachiral honeycombs hand-built in polystyrene [23]. Chiral and anti-chiral topologies of planar honeycombs have been analyzed by means of quasi-static experimental tests on small-size samples manufactured using selective laser sintering rapid prototyping of nylon powder. The experimental results have been successfully compared with the static response simulated by finite element models and simplified analytical formulations [24]. Satisfying agreement has been achieved in terms of global elastic properties (Young modulus and Poisson ratio) for almost all the studied topologies, including those exhibiting auxeticity along certain tested directions. The research findings have left some open issues regarding the tetrachiral material, exhibiting the highest discrepancy between numerical results and experimental evidences. Indeed, the numerical finite element simulations have been found to strongly overestimate the magnitude of the Poisson ratio obtained from experimental measures. In the same research field, successful comparisons between experiments and simulations on medium size samples have been also obtained for rapidly prototyped chiral honeycombs in terms of transverse shear stiffness [25], and laser-crafted re-entrant anti-trichiral honeycombs in terms of Young moduli and Poisson ratios [26].

More recently, honeycomb sheets with chiral and anti-chiral cellular topologies have been employed to develop three-dimensional curved structures. The auxeticity has been numerically simulated in microstructured cylindrical stents and experimentally verified in planar steel samples fabricated through the waterjet cutting technology [27]. Finite element results and experimental measures have been also compared to assess the coupled extensional and torsional deformations of microstructured cylindrical shells [28]. The effects of a reinforcing rotation disk introduced at the cylinder mid-height have been also considered [29]. High-pressure abrasive waterjet technologies have been applied to realize functionally graded tetrachiral structures. The influence of the geometric gradient factor on the structural elastoplastic response has been numerically predicted and experimentally analyzed during compressive load tests [30].

Negative Poisson ratios have been experimentally observed in hybrid chiral bi-dimensional materials fabricated via multi-material 3D printing. The auxeticity, combined with sequential cell-opening mechanisms, has been designed to develop multi-functional composites, featured by smart sensitivity to environmental conditions and targeted to technological applications in drug delivery and colour changing for camouflage [31]. New topologies for 3D auxetic material have been based on multi-layered tetrachiral schemes, with inter-layer clockwise and anti-clockwise ligament connections. By tuning the direction of the interlayer connections, materials with two positive and one negative Poisson ratios have been first analytically predicted and successively confirmed through numerical simulations and experimental tests on medium-size samples printed with the stereolithography technology [32]. Other topologies of 3D chiral materials have been proposed and their deformation mechanisms have been experimentally studied through tensile and compression tests on selected laser sintered samples [33].

The most notable trend emerging from the review of the most recent state-of-the-art is the increasing and pervasive employment of additive manufacturing solutions for the engineering-oriented application of the large amount of theoretical knowledge about auxetic materials based on tailorable microstructures [34–37]. Indeed, additive manufacturing is rapidly evolving as one of the most promising manufacturing technologies for designing, optimizing, rapid prototyping and large scale producing three-dimensional architected cellular materials with high-fidelity realization of complex microstructural topologies [38–42]. Interesting advanced applications for additive manufactured architected materials range across many modern fields in frontier engineering, from micro-electro-mechanical systems to lightweight components for automotive or aerospace industry, from patient-specific medical implants to smart structural elements in parametric engineering and architecture.

The additive manufacturing process always starts from a virtual 3D model that has to be converted into a 3D printing-suitable format. Then, a slicing procedure is performed and, for each slice, specific machine instructions are defined to govern the 3D printer during the layer by layer production process. Among the others, one of the most widespread, versatile, and economic 3D printing processes is the Fused Deposition Modeling (FDM). This technology employs a thermoplastic material that is first heated to a semi-molten state and then extruded through a robotically-controlled nozzle in a temperature-controlled environment to construct layer by layer the desired sample. Currently, different thermoplastic materials can be extruded, ranging from acrylonitrile butadiene styrene (ABS) and polylactic acid (PLA) to techno-polymers, like polyetherether ketone (Peek) or polytherimide (Ultem). Thanks to their superior mechanical properties, these thermoplastics can be used to produce also structural components that, by virtue of the relatively low-cost of the technology, can be used for a number of advanced technological applications ranging from acoustics and mechanics [43,44] to biomedicine and pharmaceutics [45,46], from electronics [47,48] to social applications [49,50].

This stimulating and challenging scenario motivates the leading idea to conjugate the most recent progresses in additive manufacturing with the pressing demand to establish a robust experimental background supporting the most advanced theoretical and applied researches in the exotic elasticity and smart engineering functionality of existing and new architectured materials. According to these basic motivations, the paper leverages the actual technological possibility in realizing high-fidelity complex topologies by 3D printing thermoplastic materials in order to bridge the scientific gap between analytical or numerical predictions and experimental evidences in the field of chiral microstructured materials. Focus is laid on experimentally validating

some theoretical results about the directional auxeticity of the tetrachiral material [26,51,52]. In this respect, planar polymeric samples have been 3D printed by employing the FMD technology (Section 2), in order to realize a tetrachiral cellular geometry with the highest possible precision (Section 2.1). Following a multidisciplinary approach for the data acquisition and processing, the samples have been tensile tested and the quasi-static response has been measured by means of non-contact technologies based on digital image acquisition (Section 2.2). Therefore, the measures have been analyzed by virtue of numerical data post-processing to solve the inverse problem concerned with the input-output identification of the global elastic properties (Section 2.3). In parallel, different mechanical models of the tetrachiral samples have been developed (Section 3), in the framework of solid mechanics and structural mechanics (Section 3.1). Analytical and numerical solutions have been determined to simulate the experimental tests and compare the respective findings in terms of global Young modulus and Poisson ratio (Section 3.2). As valuable point of novelty, the research outcomes have led to the theoretical conceptualization, mechanical modelization and analytical/numerical simulation of an original by-layered topology, based on tetrachiral layers. The new topology, which differs from other layered auxetic materials based on radially foldable microstructure [53] and does not require a different bi-layered multi-material 3D printing process, is kinematically based on the independent and opposite-sign *rolling-up* mechanisms of the component layers, reciprocally constrained at the boundaries. The theoretical predictions and the experimental behaviour have been compared in terms of global rigidity and auxeticity (Section 4). Finally, concluding remarks have been pointed out and future developments have been outlined. Further information about (i) the geometric properties of the tested samples and the loading steps of the experimental tests (Section A.1), (ii) the identification of the global elastic properties (Section A.2), (iii) the mechanical formulations for the tetrachiral and bi-tetrachiral models (-Section B) are extensively reported in the Supplementary Material.

2. Tetrachiral sample

The class of chiral and antichiral cellular materials is characterized by a periodic tessellation of the bidimensional plane. The elementary cell is strongly characterized by a microstructure composed by stiff circular rings connected by flexible straight ligaments, arranged according to different planar geometries including the trichiral, hexachiral, tetrachiral, anti-trichiral, anti-tetrachiral topologies. Among the others, the tetrachiral material is featured by a monoatomic centrosymmetric cell in which the central stiff and massive ring (or disk) is connected to four tangent flexible and light ligaments.

2.1. Sample preparation

A polymeric sample of the tetrachiral geometry has been realized with Fused Deposition Modeling (FDM) technology by the Group of Computational Mechanics and Advanced Materials of the University of Pavia (Fig. 1). For the layer-by-layer FDM preparation of the samples a thermoplastic filament made of the polymer Acrylonitrile Butadiene Styrene (ABS) has been used. This material has a Young modulus ranging in the large interval 1100–2900 MPa. In the initial pre-print conditions, the nominal value given by the filament manufacturer is close to 2000 MPa. The reduced value for the post-print conditions is a matter of experimental identification and has been tentatively fixed at 1300 MPa as initial realistic value. The Poisson ratio has been realistically fixed at the nominal value of 0.35.

The printing head movements and all the printing parameters are automatically controlled by an electronic board relying on a set of instructions (i.e., the G-Code). The G-Code is produced by a dedicated software, commonly called *slicer* or *slicing software* that takes into account the virtual geometry, the properties of the printing material, and the specific features of the 3D-printer. The 3D printer used to produce the tetrachiral sample was a 3NTR A4v3 (see Fig. 1a,b). The
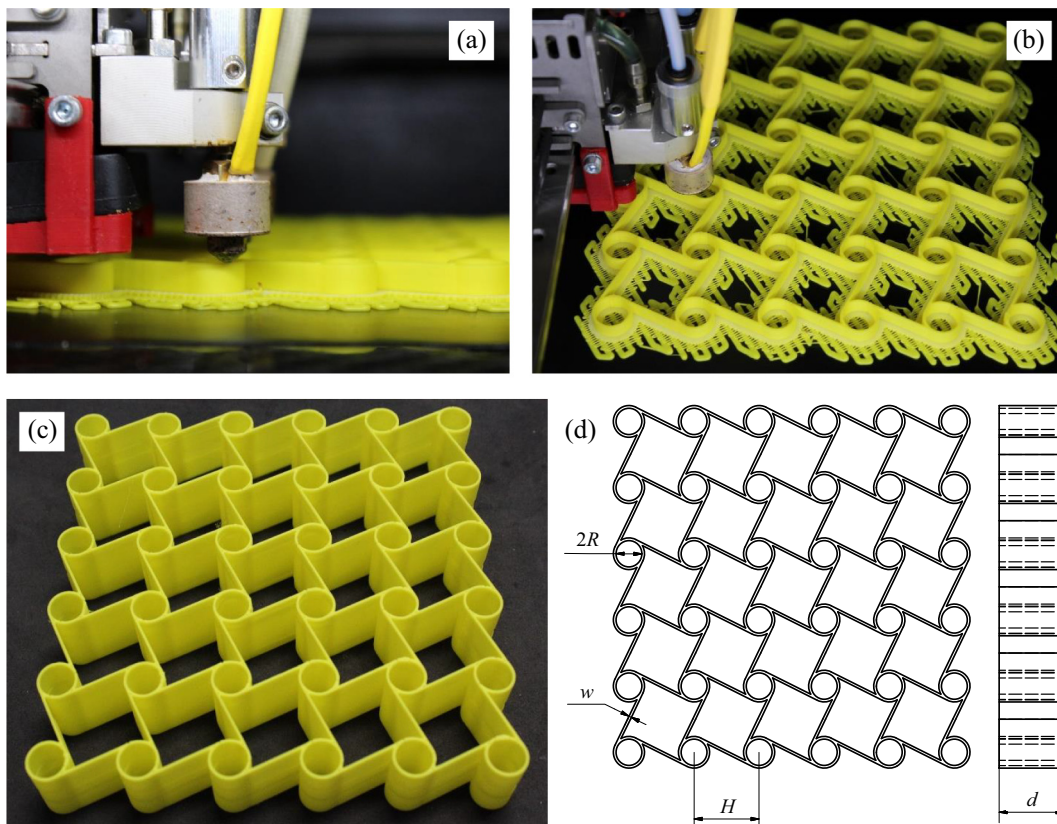

Fig. 1. Tetrachiral sample printed with the FDM technology: (a), (b) 3NTR 3D printer preparing the tetrachiral sample; (c) 3D printed sample; (d) geometry of the printed sample.

machine has been equipped with three extruders that can be heated up to 410 °C; a nozzle of 0.4 mm of diameter has been used. The build-tray temperature has been set to 110 °C, while the heated chamber temperature to 70 °C in order to avoid distortions of the printed sample induced by the high thermal gradients occurring during the manufacturing process. A filament cross-section with thickness of 0.2 mm and width of 0.4 mm, and a fiber-to-fiber overlap of 0.04 mm has been assumed [54]. The printer sample and its geometry are reported in Fig. 1c,d and detailed in Table 1 of Section A.1 of the Supplementary Material.

2.2. Experimental tests

The experimental activities have been carried out at the Laboratory of Structural Engineering of the DICCA – University of Genova. The tetrachiral samples made of an array of 6-by-6 cells have been tested under uni-axial tension according to a force-control scheme, within stable environmental conditions (Fig. 2a). The test set up has been designed to apply known increments of force to the sample, starting from an initial reference configuration.

In the reference configuration, the sample is hanging vertically under self-weight load and supported by a constraining system applied at the top side (Fig. 2b). The constraining system has been purposely designed to ideally preserve the alignment of all the rings located in the first (top) row of the sample (yellow-filled black rings in Fig. 2b). The transversal displacements and rotations of all the rings remain ideally free, allowing the unrestricted development of both lateral expansion/contraction and the *rolling-up* mechanism. The controlled force acts at the bottom side of the sample by means of a steel truss system conveniently designed to split the total vertical action into equal forces (red vectors in Fig. 2b) applied at all the rings located in the last (bottom) row of the sample (pink-filled black rings in Fig. 2b). In order to assess the global elastic properties of the tetrachiral sample, the 4-by-6 inner cluster of internal unconstrained and unloaded cells (green region in Fig. 2b) been considered in the following.

The uni-axial tension test has been run by applying five increments of the quasi-static force F_2, corresponding to equivalent global stress $\Sigma_{22} = F_2/A_2$, where $A_2 = 6Hd$ is the cross-section area of the ideal solid (rectangular parallelepiped) with dimensions $6H$ (width), $6H$ (height) and d (depth). The force increments (steps 1–5) are detailed in Table 2 (reported in the Section A.1 of the Supplementary material), starting from the initial loading conditions (step 0) under the self-weight of the sample and the truss system. Particular attention has been payed to some operational issues, like preserving the vertical

planarity of the deformed configurations and minimizing the parasitic effects of friction in the constraints. Finally, the entire loading process has been assumed not to overcome the limit of linear reversible deformation at the global scale of the tetrachiral sample. This assumption has been checked a posteriori by verifying that the initial undeformed configuration is macroscopically recovered at the end of the unloading process, here not reported for the sake of synthesis.

2.3. Data processing and identification of the global elastic properties

Among the different available possibilities for data recording in quasi-static experimental tests, the non-contact data acquisition through a digital camera has been selected as a convenient compromise between measure reliability and operational feasibility. Specifically, one or more two-dimensional images (with dimensions 5184-by-3456 pixels) of the tetrachiral specimen have been acquired for each load step with a fixed camera (14 bit Canon EOS 600D, with image processor DIGIC 4). In order to minimize distortion, the focal plane of the digital camera has been initially calibrated to be parallel to the specimen plane, with the focal axis crossing the geometric center of the specimen in the undeformed configuration.

All the digital photographs have been uploaded and converted in two-dimensional arrays of pixel coordinates within the Matlab environment, in order to be post-processed by using the Image Processing Toolbox. First, the background grid of known dimensions (approximately co-planar with the specimen) has been employed to convert the pixel coordinates of the digital photograph into a real coordinate system. Second, the real positions **x** of the ring centers have been assessed by programming an automatic function for the recognition of assigned shapes, based on the Hough transform. This mathematical transform is an efficient tool for geometric shape recognition, largely used in digital image processing and computer vision. The automatic recognition of an assigned shape is based on searching object imperfections within a certain class of geometric objects, in which the most suited candidates are recognized as local maxima in a finite parameter space (also known as accumulator space). In this respect, the Hough transform, which is classically concerned with the identification of lines in digital images, can be easily extended to identify the centers and radii of circular curves.

By properly tuning the sensitivity parameters of the automatic function, the identification of the real coordinates of all the unconstrained ring centers in the tetrachiral specimen has been successfully run for each load step (Fig. 3). Therefore, the total displacements of the ring centers have been calculated as position differences with respect to
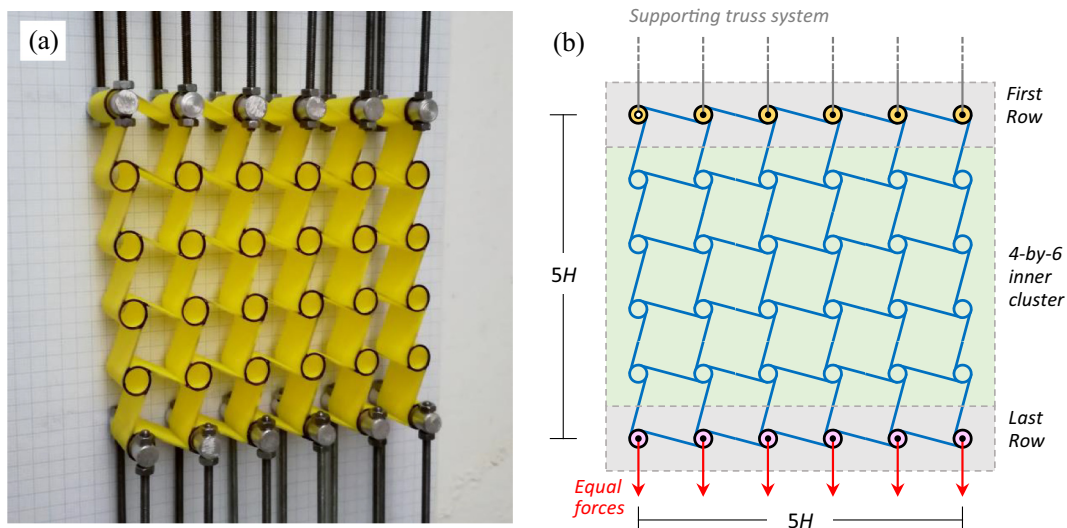

Fig. 2. Experimental set up in the initial reference configuration: (a) picture, (b) sketch of the supported tetrachiral sample under the action of the external forces.
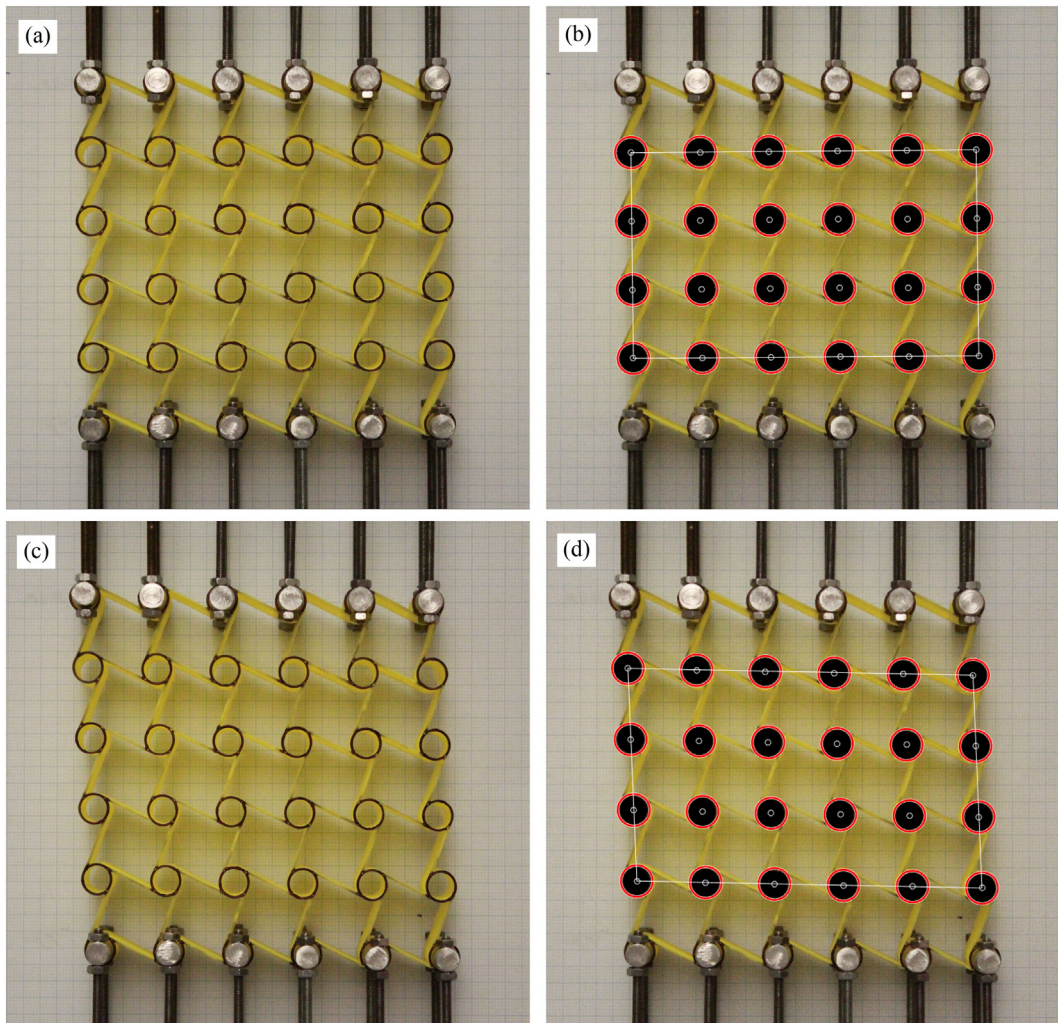
Fig. 3. Non-contact image-based identification of the real coordinates for all the ring centers in the inner cluster of the tetrachiral sample: (a), (b) loading step 0; (c), (d) loading step 5.

the initial load step, and the results have been stored in the experimental set of punctual displacement vector **v**.

According to a mechanical model-based identification, the global elastic properties of the tetrachiral samples have been identified by introducing the in-plane affine displacement field $\mathbf{u}(\mathbf{x})$ of an equivalent homogeneous Cauchy continuum in the framework of a linear kinematics (Fig. A in the Supplementary Material). Hence, the identification

procedure has been based on the least square solution of the overdetermined inverse kinematic problem derived from the formal mathematical analogy between the model-based linear kinematic law $\mathbf{u}(\mathbf{x}) = \mathbf{u}_0 + \mathbf{H}\mathbf{x}$ for the continuous displacement variable $\mathbf{u}(\mathbf{x})$ and the data-driven linear regression law $\mathbf{v}(\mathbf{x}) = \mathbf{v}_0 + \mathbf{G}\mathbf{x}$ extracted from the displacement data **v** measured at the positions **x**. The identification procedure is reported in details in Section A.2 of the Supplementary Material.
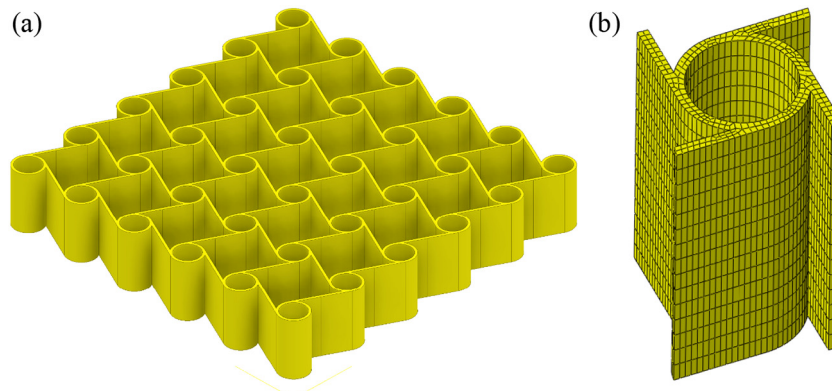

Fig. 4. Three-dimensional solid model of the tetrachiral sample: (a) perspective geometric view of the six-by-six cell sample; (b) detail of the finite element mesh for the periodic cell.

3. Numerical simulations and analytical predictions

3.1. Solid finite element model and beam lattice model

The tetrachiral samples can be modelled according to a high-dimensional formulation in the framework of linear solid mechanics. The software Autodesk Inventor has been used as CAD modeling tool to describe with high-fidelity the complex three-dimensional geometry of the generic tetrachiral samples composed by a bidimensional array of $N \times M$ cells, with N rows and M columns (Fig. 4a illustrates the six-by-six cell sample). Therefore, the software Abaqus Standard has been used as finite element mesh generator and solver. The entire sample domain has been discretized with 8-node linear brick, reduced integration, hourglass control (C3D8R) elements. The six-by-six cell sample has been meshed in 146220 brick elements and the mesh detail of the periodic cell are illustrated in Fig. 4b. Details about the definition of the material properties, the boundary conditions and the inter-layer constraints are reported in Section B.1 of the Supplementary Material.

As an alternative to the high-dimensional solid model, the periodic cell of the tetrachiral samples can be modelled according to a low-dimensional lagrangian formulation in the framework of linear mechanics (Fig. 5a). The tetrachiral planar geometry is characterized by the side length H of the periodic square cell and the mean radius R of the rings (Fig. 5b). According to simple trigonometric considerations, the chirality angle of the tangent ligaments is $\beta = \arctan(2R/H)$ and the ligament length is $L = H \cos \beta$. The lagrangian model is synthesized in a suited parametric form on the base of a few mechanical assumptions. The stiff rings are conveniently described as annular rigid bodies, while the flexible ligaments are described as unshearable beams. A linear elastic material with Young modulus E is assumed for all beams. Therefore, each beam is characterized by axial rigidity EA and in-plane flexural rigidity EJ. Moreover, the beam-annulus connections are assumed perfectly rigid joints. Details about the parametric stiffness matrices governing the equilibrium equations are reported in the Section B.2 of the Supplementary Material.

3.2. Comparison of experiments and simulations

The experimental results are compared qualitatively and quantitatively with the simulations obtained with the lagrangian model and with the finite element solid model of the tetrachiral sample. First, from a qualitative point of view, all the experimental deformed configurations (see for instance Fig. 3c) and the corresponding static simulations agree in exhibiting a non-symmetric behaviour in response to the application of the symmetric scheme (with respect to the vertical in-plane axis crossing the sample barycenter) of external forces. This behaviour can be essentially attributed to the chirality of the cellular topology, which determines the development of local deformation

mechanisms, activated by the rotation of the rings around their centers (*rolling-up*). Globally, the vertical stretching of the sample – collinear to the external force direction – is accompanied with an evident and significant angular strain. This characteristic behaviour is observable in the deformed configurations obtained from the experimental test (Fig. 3d), as well as in the numerical simulations obtained from the solid model (Fig. 6). It is worth noting that the sign of the angular strain is univocally related to the sign of the chirality angle in the cellular topology (angle β in Fig. 5b). For the numerical simulations, the horizontal component of the normalized displacement field $U/U_{\max}$ is shown in Fig. 6a, while the deformed and undeformed configurations are compared in Fig. 6b,c.

Second, from a quantitative point of view, the normal and angular strains identified starting from the experimental data are compared with the corresponding strains identified starting from the numerical results obtained with the Lagrangian and the finite element solid models, respectively (Fig. 7). As a major remark, it can be noted that the experimental response (red circles) shows – with a good approximation – a linear behaviour under increasing values of the external forces. With focus on the solid model, it can be observed that the ratio Σ_{22}/E_{22} obtained from the numerical results (blue circles in Fig. 7a) systematically underestimates the corresponding experimental ratio (red circles). This occurrence has demonstrated the need to update the nominal value initially assumed for the Young modulus of the ABS material (1300 MPa), which has been recognized as the most uncertain mechanical parameter according to the initial information available. Therefore, this parameter has been properly updated in order to zeroing the difference between the global Young modulus E identified from the numerical results (load-independent value marked by green circles in Fig. 8a) and the average of the global Young modules ($E = 1.02$ MPa), identified from the experimental results at different loading steps (red circles in Fig. 8a). The updating procedure has required an increment in the Young modulus of the ABS material of about 18% (up to 1540 MPa). The ratio Σ_{22}/E_{22} obtained from the numerical results of the updated solid model (green circles in Fig. 7a) shows a better agreement with the corresponding experimental ratio (red circles).

Adopting the updated solid model, a very satisfactory agreement is achieved between the ratio E_{11}/E_{22} obtained from the numerical results (green circles or, rigorously, the slope of the dashed line connecting the green circles in Fig. 7b) and the corresponding experimental ratio (red circles or, rigorously, slope of the dashed line linearly regressing the red circles in Fig. 7b). The negative value systematically attained by this ratio for increasing external forces demonstrates a non-auxetic behaviour of the tetrachiral sample in the direction orthogonal to the external forces. This key result is effectively synthesized by the positive values systematically identified for the global Poisson ratio ν (Fig. 8b). In particular, the load-independent value ($\nu = 0.27$) identified from the numerical results (green circles in Fig. 8b) closely matches the
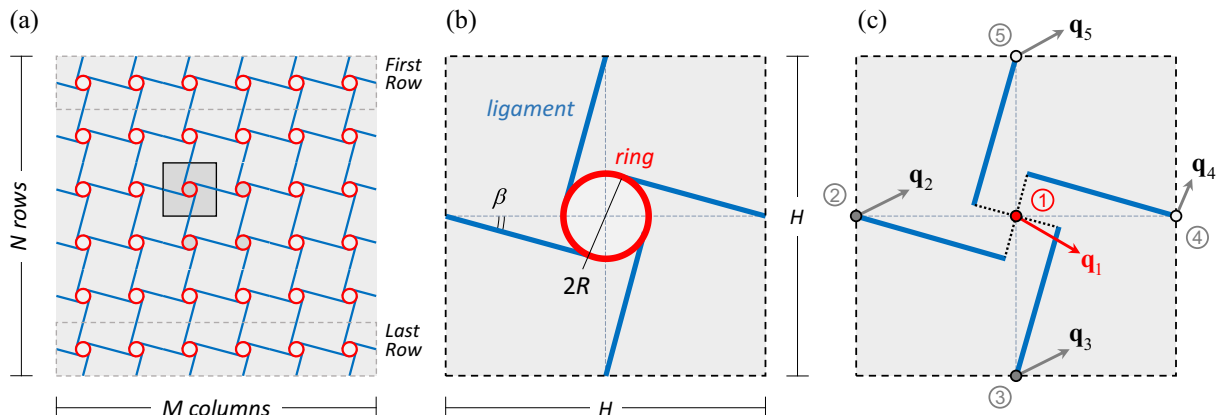

Fig. 5. Tetrachiral sample: (a) repetitive planar pattern, (b) periodic cell, (c) beam lattice model.
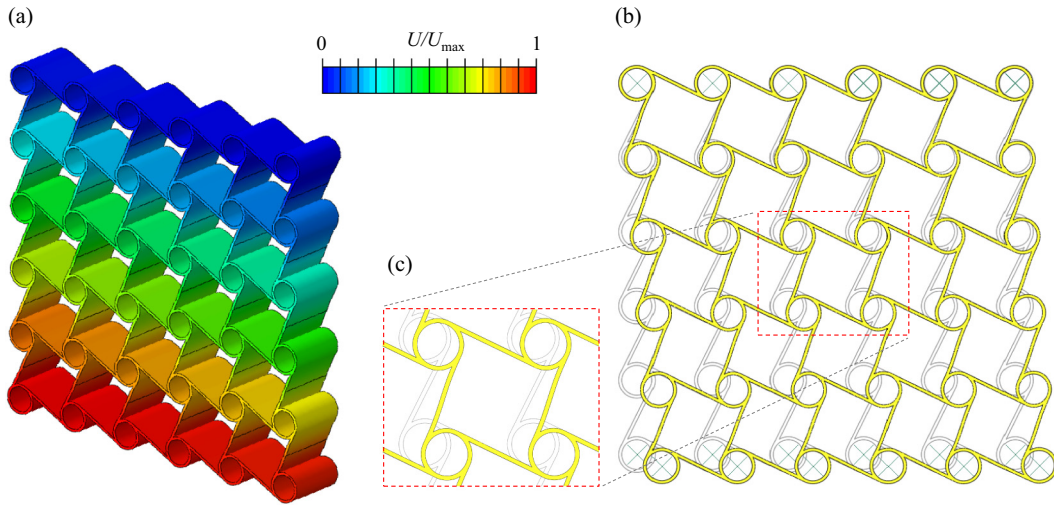
Fig. 6. Finite element simulation of the tetrachiral sample: (a) colour map of the horizontal displacement component; (b), (c) comparison between the undeformed (gray lines) and deformed configuration (yellow solid). (For interpretation of the references to colour in this figure legend, the reader is referred to the web version of this article.)

mean value ($\nu = 0.26$) identified from the experimental results (red circles in Fig. 8b). It is worth noting that these two consistent values are also in good agreement with the analytical results obtained from a second gradient continuum model of the tetrachiral material formulated according to a proper homogenization technique [51]. Finally, the first qualitative remark concerned with the development of a non-negligible angular strain is quantitatively confirmed by the identification of the strain E_{12} that assumes experimental and numerical values in mutual agreement and quantitatively comparable with the values of the normal strain E_{22} (green and red circles in Fig. 7c).

With focus on the Lagrangian model, a good matching is found in the simulation (yellow circles in Fig. 7a) of the experimental ratio Σ_{22}/E_{22}. Differently, the global Young modulus identified from the Lagrangian simulation (load-independent value marked by yellow circles in Fig. 8a) returns a slight underestimation ($E = 0.94$ MPa) of the mean experimental value (red circles in Fig. 8a). This difference is a well-established finding that can be attributed to the rigid body assumption for the central ring and to the overestimation of the effective length in the flexible ligaments composing the cellular microstructure [51]. Furthermore, the simplifying assumptions of the Lagrangian formulation do not allow the accurate assessment of the experimental value for the ratio E_{11}/E_{22} (compare red and yellow circles in Fig. 7b). Indeed, it can be highlighted that the corresponding load-independent identification of the global Poisson ratio ($\nu \approx 0$ marked by yellow circles in Fig. 8b) is perfectly consistent with the null value ($\nu = 0$) exactly obtainable by the static condensation (returning a first-order model) of a micropolar continuum model of the tetrachiral material, formulated according to a proper continualization technique [51]. In contrast, the

Lagrangian model accurately captures the positive experimental ratio E_{12}/E_{22} (yellow circles in Fig. 7c), which measures the coupling between the normal strain E_{22} and the angular strain E_{12}.

4. Bi-tetrachiral sample

4.1. Sample preparation, Experimental set-up, Data acquisition and processing

The bi-layered polymeric sample of the bi-tetrachiral geometry has been obtained by simply superimposing two tetrachiral samples (front and back layers) with opposite chirality. The geometry of the samples is detailed in Table 1 (Section A.1 of the Supplementary material).

As for the tetrachiral samples, bi-tetrachiral samples made of an array of 6-by-6 cells have been experimentally tested under uni-axial tension according to the force-control scheme, under stable environmental conditions. Known increments of force have been applied to the sample, starting from the initial constrained configuration (Fig. 9a), taken as reference. In the reference configuration, the sample lies in the vertical plane under self-weight load and is supported by the alignment-preserving constraining system. The supporting system is designed to constrain the relative displacements (but not the relative rotation) of all the 6 ring pairs (one ring in the front layer, the other in the back layer) at the top side. The steel truss system acting at the bottom side of the bi-tetrachiral sample applies the controlled force and simultaneously constrains the relative displacements (but not the relative rotation) of all the 6 ring pairs (one ring in the front layer, the other in the back layer) at the bottom side. The total vertical action is
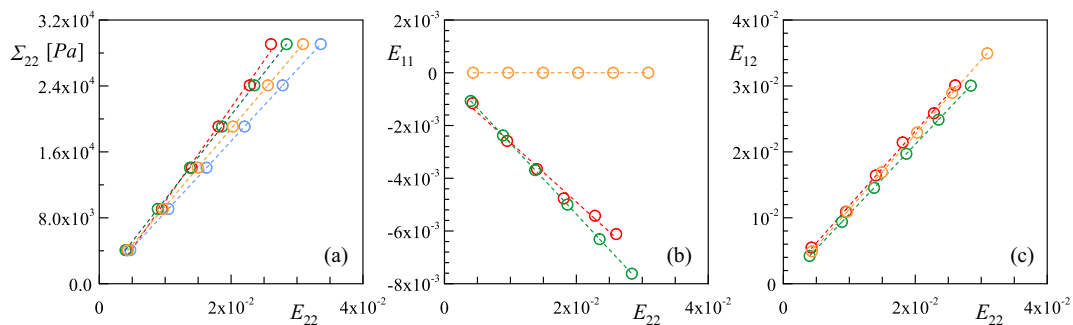

Fig. 7. Comparison between experimental results (red circles) and numerical results of the solid model (blue and green circles) and beam lattice model (yellow circles): (a) equivalent global stress Σ_{22} versus normal strain E_{22}, (b) normal strain E_{11} versus normal strain E_{22}, (c) angular strain E_{12} versus normal strain E_{22}. (For interpretation of the references to colour in this figure legend, the reader is referred to the web version of this article.)
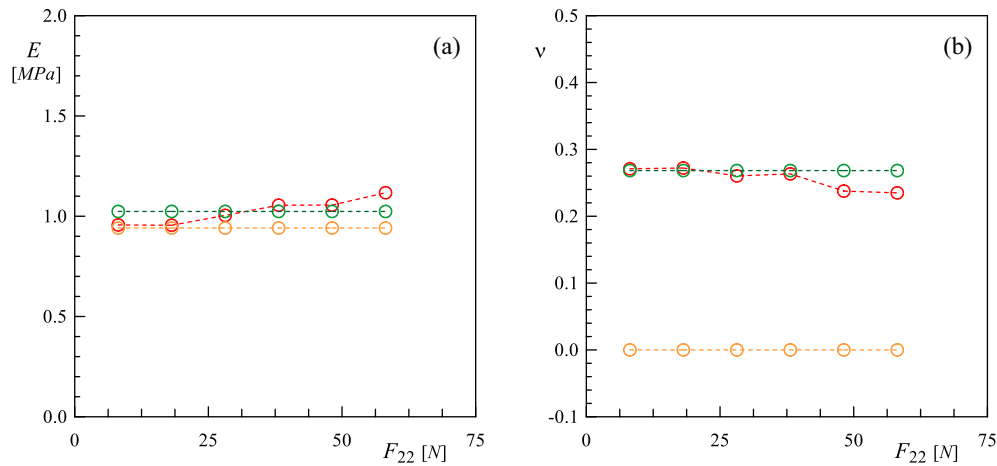
Fig. 8. Comparison between experimental results (red circles) and numerical results of the solid model (green circles) and beam lattice model (yellow circles). Global elastic properties versus external load F_{22}: (a) Young modulus E, (b) Poisson ratio ν. (For interpretation of the references to colour in this figure legend, the reader is referred to the web version of this article.)

split into equal forces applied at all the ring pairs located in the last (bottom) row of the sample (Fig. 9b). Apart from the relative constraints at the top and bottom sides, each layer is free to independently develop its own lateral expansion/contraction, as well as its own *rolling-up* mechanism. In order to assess the global elastic properties of the bi-tetrachiral sample, the 4-by-6 inner cluster of internal unconstrained and unloaded cells (green region in Fig. 9b) has been considered in the following.

The uni-axial tension test has been run by applying five increments of the quasi-static force F_2, corresponding to equivalent global stress $\Sigma_{22} = F_2/A_2$, where $A_2 = 12Hd$ is the cross-section area of the ideal solid with dimensions $6H$ (width), $6H$ (height) and $2d$ (depth). The force increments (steps 1–5) are the same already detailed in Table 2 (reported in Section A.1 of the Supplementary Material), starting from the initial configuration (step 0). Attention has been paid to preserve the vertical planarity of the deformed configurations, minimizing as much as possible the undesired effects of friction in the constraints and not overcoming the limit of linear reversible deformation at the global scale of the material sample.

As for the tetrachiral samples, the non-contact data acquisition has been performed through a digital camera. Specifically, one or more two-dimensional images (with dimensions 5184-by-3456 pixels) of the bi-tetrachiral specimen have been acquired for each load step, taking care of minimizing distortion by properly calibrating the focal axis

and focal plane of the camera according to the specimen plane and geometry. After uploading the digital photographs in the Matlab environment, the Image Processing Toolbox has been employed to convert the pixel coordinates of the digital photograph into a real coordinate system. The real positions $\mathbf{x}$ of the ring centers of the layers have been again assessed by recognizing the circular shapes by virtue of the Hough transform for each load step. Therefore, the total displacement vector $\mathbf{v}$ of the ring centers have been calculated as position differences with respect to the initial load step. Finally, the global elastic properties (Young modulus E and Poisson ratio ν) have been identified according to the procedure outlined in Section 2.3 and more extensively reported in Section A.2 of the Supplementary Material.

4.2. Numerical simulations and analytical predictions

In analogy with the tetrachiral samples, the bi-tetrachiral samples can be modelled according to a high-dimensional formulation in the framework of linear solid mechanics. The two layers have been first reproduced with high geometrical fidelity in the framework of the CAD tool (Fig. 10a illustrates the six-by-six cell sample), and successively discretized and analyzed using Abaqus. The same mesh size and the element type of the tetrachiral solid model have been adopted for the two layers of the bi-tetrachiral samples (for instance, the six-by-
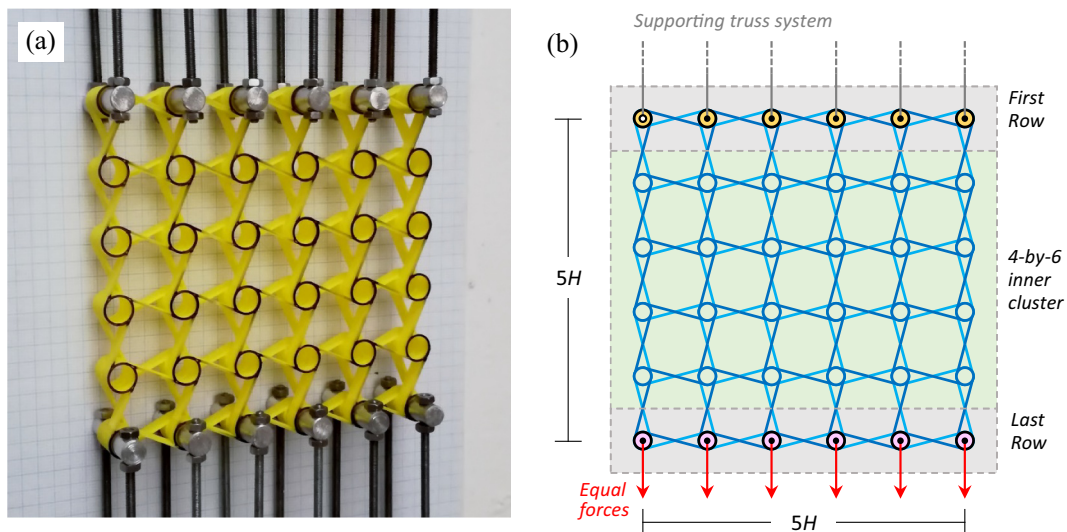

Fig. 9. Experimental set up in the initial reference configuration: (a) picture, (b) sketch of the supported bi-tetrachiral sample under the action of the external forces.
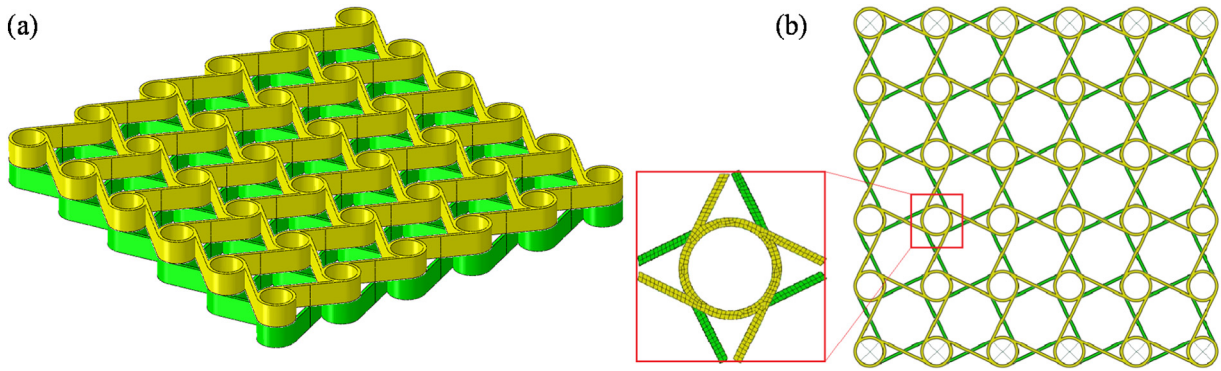
Fig. 10. Three-dimensional solid model of the bi-tetrachiral sample: (a) perspective geometric view of the six-by-six cell sample; (b) finite element mesh and detail of the periodic cell.

six cell sample has been meshed in 129834 C3D8R elements and the mesh detail of the periodic cell are illustrated in Fig. 10b). The material properties, the boundary conditions and the inter-layer constraints are reported in Section B.3 of the Supplementary material.

As an alternative to the high-dimensional solid model, the bi-layered periodic cell of the bi-tetrachiral samples can be modelled according to a low-dimensional lagrangian formulation in the framework of linear mechanics (Fig. 11a). For each layer, the independent geometric properties of the periodic square cell are the side length H and the ring radius R. The chirality angles of the tangent ligaments are $\beta = \pm$ arctan $(2R/H)$, where the positive and the negative signs correspond to the front layer and to the back layer, respectively (Fig. 11b). Based on the simplifying mechanical assumptions already introduced for the lagrangian model of the tetrachiral samples, identical structural properties (stiff rings, flexible ligaments with Young modulus E, axial and flexural rigidities EA and EJ) are considered for the two layers of the bi-tetrachiral samples. In the reference planar configuration, the two internal nodes (one for each layer) and the eight external nodes (four for each layer) share the same position. Details about the parametric stiffness matrices governing the equilibrium equations are reported in the Section B.4 of the Supplementary Material.

4.3. Comparison of experiments and simulations

The experimental results are compared qualitatively and quantitatively with the simulations obtained with the lagrangian and the finite element solid model of the bi-tetrachiral sample. First, from a qualitative point of view, the two layers exhibit a different but mutually and doubly symmetric behaviour in all the experimental deformed configurations under the symmetric scheme of external forces. Specifically, the response of the two-layer sample is symmetric with respect to the vertical and horizontal in-plane axes crossing the sample barycenter. The

double symmetry of the experimental response is confirmed by the static simulations. This peculiar behaviour can be essentially attributed to the opposite chiralities of the two layers composing the cellular topology. The opposite chirality angles determine the concurrent development of two independent *rolling-up* mechanisms of local deformation, one for each layer, activated by the opposite-sign rotations of the rings around their centers. Globally, the vertical stretching of the sample – collinear to the external force direction – is not accompanied with any appreciable angular strain. This characteristic behaviour is observable in the experimental deformed configurations, as well as in the numerical simulations obtained from the solid model (Fig. 12).

The horizontal component of the normalized displacement field $U/U_{\max}$ is shown in Fig. 12a, while the deformed configurations of the front layer (yellow) and back layer (green) are portrayed in Fig. 12b,c. Second, from a quantitative point of view, the normal and angular strains identified from the experimental data are compared with the corresponding strains identified from the numerical results obtained with the lagrangian and the finite element solid models (Fig. 13), respectively. As for the tetrachiral sample, it can be noted that the experimental response (red circles) shows a quasi-perfectly linear behaviour under increasing values of the external forces.

With focus on the solid model, which employs the updated Young modulus of the ABS material (1540 MPa), the ratio Σ_{22}/E_{22} obtainable from the numerical results of the updated solid model (green circles in Fig. 13a) shows a fine agreement – apart from a minor underestimation – with the corresponding experimental ratio (red circles in Fig. 13a). Consistently with this remark, the global Young modulus ($E = 2.11$ MPa) identified from the numerical results (green circles in Fig. 14a) is slightly lower than the minimum and the mean value ($E = 2.26$ MPa) of the global Young modules identified from the experimental results (circles reds in Fig. 14a). In synthesis, it can be highlighted how the global Young modulus of the bi-tetrachiral sample
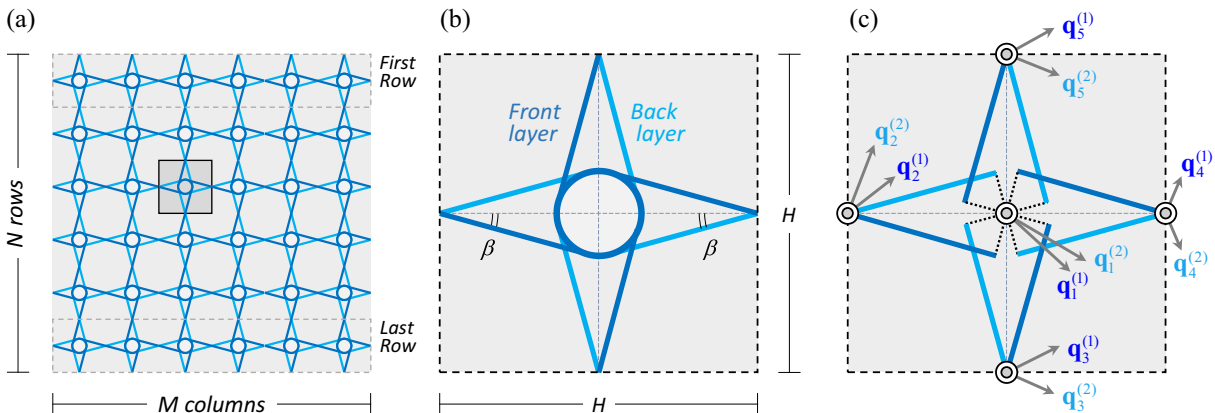

Fig. 11. Bi-Tetrachiral sample: (a) repetitive planar pattern, (b) periodic cell, (c) beam lattice model.
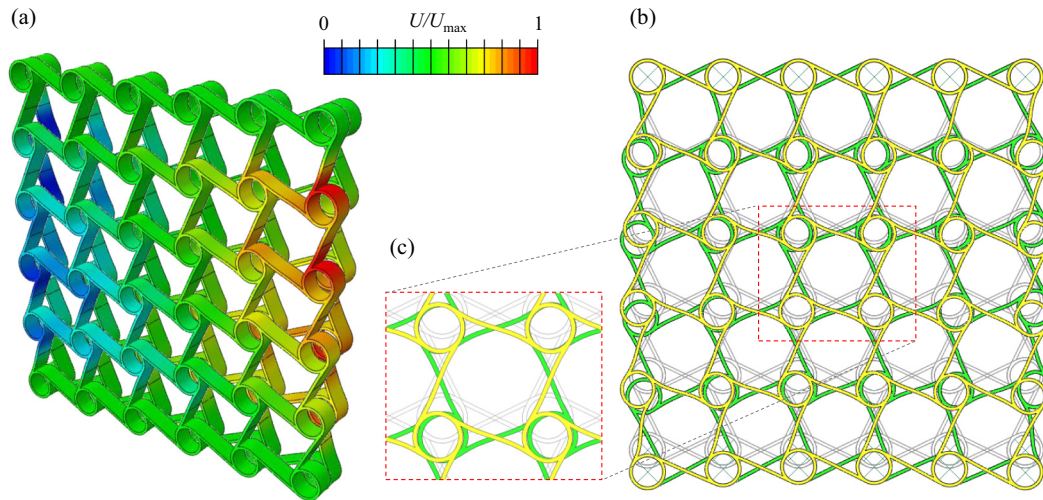
Fig. 12. Finite element simulation of the bi-tetrachiral sample: (a) colour map of the horizontal displacement component; (b), (c) comparison between the undeformed (gray lines) and deformed configuration (yellow and green solids). (For interpretation of the references to colour in this figure legend, the reader is referred to the web version of this article.)

– in virtue of the two layer collaboration – is about twice that of the tetrachiral sample made of the same material.

Adopting the updated solid model, a very satisfactory agreement is again achieved between the ratio E_{11}/E_{22} obtained from the numerical results (green circles in Fig. 13b) and the corresponding experimental ratio (red circles). However, the positive values systematically attained by this ratio for increasing external forces demonstrate a remarkably auxetic behaviour of the bi-tetrachiral sample in the direction orthogonal to the external forces. This key result fundamentally differentiates the global behaviour of the bi-tetrachiral material from that of the tetrachiral material individually characterizing the two component layers. From a mechanical perspective, this drastic change in the static response can be fully attributed to the inter-layer rigid constraint at the boundaries (top and bottom cell rows). The auxetic behaviour is effectively synthesized by the negative values systematically identified for the global Poisson ratio ν (Fig. 14b). In particular, the load-independent value ($\nu = -0.71$) identified from the numerical results (green circles in Fig. 14b) effectively matches – apart from a small underestimation – the mean value ($\nu = -0.64$) identified from the experimental results (red circles). Finally, the first qualitative remark concerning the absence of an appreciable angular strain is quantitatively confirmed by the identification of the angular strain E_{12}, which assumes experimental and numerical values in mutual agreement but significantly lower (by two orders of magnitude) than those of the normal strain E_{22} (green and red circles in Fig. 13c).

With focus on the lagrangian model, a satisfying agreement is found in the simulation (yellow circles in Fig. 13a) of the experimental ratio

Σ_{22}/E_{22}. The identification of the global Young modulus from the lagrangian simulations (load-independent values marked by yellow circles in Fig. 14a) returns a slight underestimation ($E = 1.98$ MPa) of the corresponding values identified from the experiments (red circles) and the finite element solid model (green circles). Similarly to the tetrachiral sample, this difference can be attributed to the simplifying mechanical assumptions of the lagrangian formulation [51]. Despite the simplifying assumptions, the lagrangian formulation allows the identification of positive values for the ratio E_{11}/E_{22}, consistently with the experimental results. Nonetheless, it can be noted that the corresponding load-independent identification of the global Poisson ratio ($\nu = -0.95$ marked by yellow circles in Fig. 14b) systematically overestimates the actual auxeticity of the bi-tetrachiral sample. Finally, the lagrangian model confirms a certain accuracy in fitting the experimental ratio E_{12}/E_{22} (yellow circles in Fig. 13c).

Once the actual reliability of the mechanical formulations in simulating the static response of the bi-tetrachiral material has been experimentally verified, the solid and the lagrangian models have been used to simulate the behaviour of square samples characterized by increasing size (up to $N = M = 18$). Given the key role played by the inter-layer boundary constraints on the auxetic response of the bi-tetrachiral material, the purpose of these simulations is targeted to verifying the influence of the boundary-to-boundary distance on the global elastic properties. Regardless of the sample size, the identification of the global Young modulus and global Poisson ratio has been based on the displacement subvector **v** related to the inner cluster of 4-by-6 cells, for the sake of consistency. The values of the global Young modulus identified from
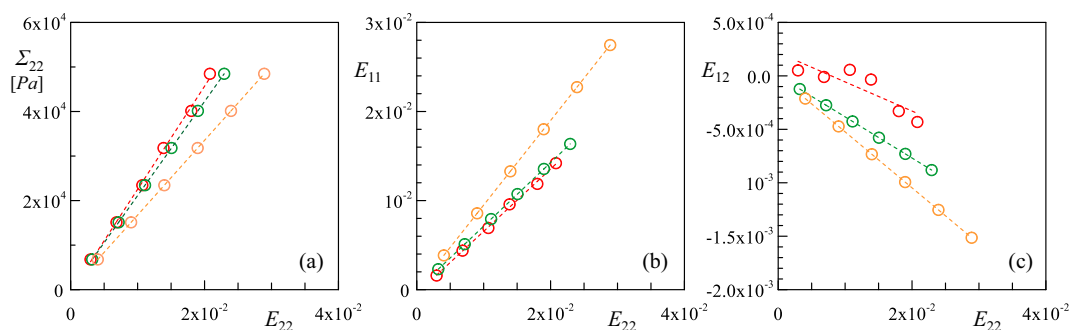

Fig. 13. Comparison between experimental results (red circles) and numerical results of the solid model (green circles) and beam lattice model (yellow circles): (a) equivalent global stress Σ_{22} versus normal strain E_{22}, (b) normal strain E_{11} versus normal strain E_{22}, (c) angular strain E_{12} versus normal strain E_{22}. (For interpretation of the references to colour in this figure legend, the reader is referred to the web version of this article.)
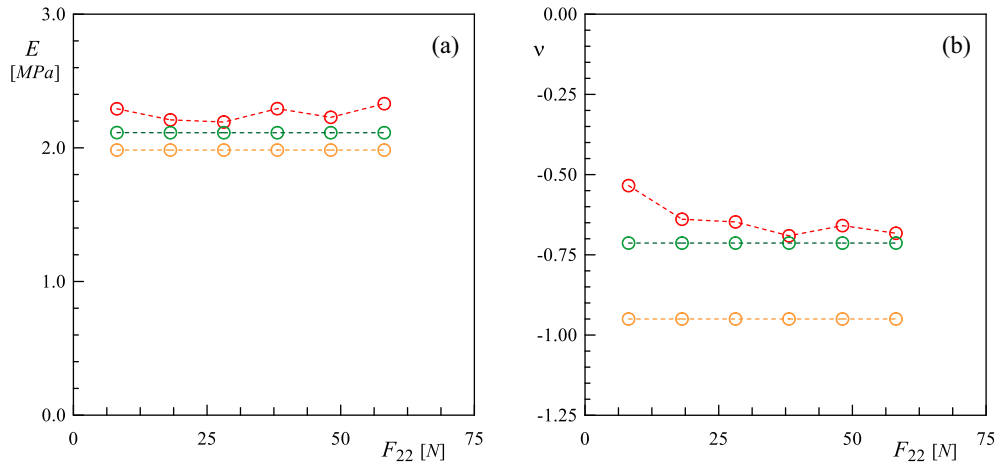
Fig. 14. Comparison between experimental results (red circles) and numerical results of the solid model (green circles) and beam lattice model (yellow circles). Global elastic properties versus external load F_{22}: (a) Young modulus E, (b) Poisson ratio ν. (For interpretation of the references to colour in this figure legend, the reader is referred to the web version of this article.)

the solid model (green circles) and from the lagrangian model (yellow circles) exhibit limited variability for increasing sizes of the samples (Fig. 15a). Specifically, E-values ranging from 2.08 MPa to 2.14 MPa have been obtained for the solid model (respectively for $N = 8$ and $N = 14$), while E-values ranging from 1.94 MPa and 1.98 MPa have been obtained for the lagrangian model (respectively for $N = 8$ and $N = 6$). Differently, the values of the global Poisson ratio identified from the solid model (green circles) and from the lagrangian model (yellow circles) exhibit a monotonically convergent behaviour for increasing sizes of the samples. For the largest size ($N = 18$) the global Poisson ratio attains the minimum values $\nu = -0.99$ for the solid model and $\nu = -1.10$ for the lagrangian model (Fig. 15b). This persistent result tends to confirm that the auxeticity is a property of the bi-tetrachiral material that actually leverages the inter-layer boundary constraints, but does not vanish for large boundary-to-boundary distances. In order to give an opportune reference with respect to known results from the existing literature, similar highly auxetic (isotropic) responses have been achieved for the hexachiral honeycombs ($\nu = -0.95$ as documented in [51]).

5. Conclusions

The global elastic properties of architectured honeycomb materials featured by a tetrachiral cellular microstructure, made of circular stiff rings tangentially connected by flexible ligaments, have been investigated. The theoretical predictions based on beam lattice formulations and finite element solid models have been compared with the experimental data obtained from quasi-static laboratory tests performed on different planar samples realized with the 3D printing technology. As major experimental evidence, the tetrachiral samples show a remarkable coupling between the normal and angular strains under increasing tension loads, due to the local ring rotations activated by the cellular chirality (*rolling-up* mechanism). For the particular test direction, the global Young modulus and the global (positive) Poisson ratio of the tetrachiral material samples, experimentally identified by solving an overdetermined inverse problem, are accurately predicted by the numerical results of the solid computational model. On the contrary, some simplifying mechanical assumptions tend to limit the actual descriptive possibilities of the beam lattice model, particularly if the ring deformability is comparable with the ligament flexibility.

Inspired by the encouraging findings concerning the tetrachiral material, an original bi-layered topology of microstructured tetrachiral materials (*bi-tetrachiral materials*) has been theoretically conceived and mechanically modelled. The bi-tetrachiral topology exploits the virtuous mutual collaboration of two tetrachiral layers with opposite chirality, in order to prevent the development of angular strains under tensile loads. As major technological advantage, the new material topology does not require a different bi-layered multi-material 3D printing
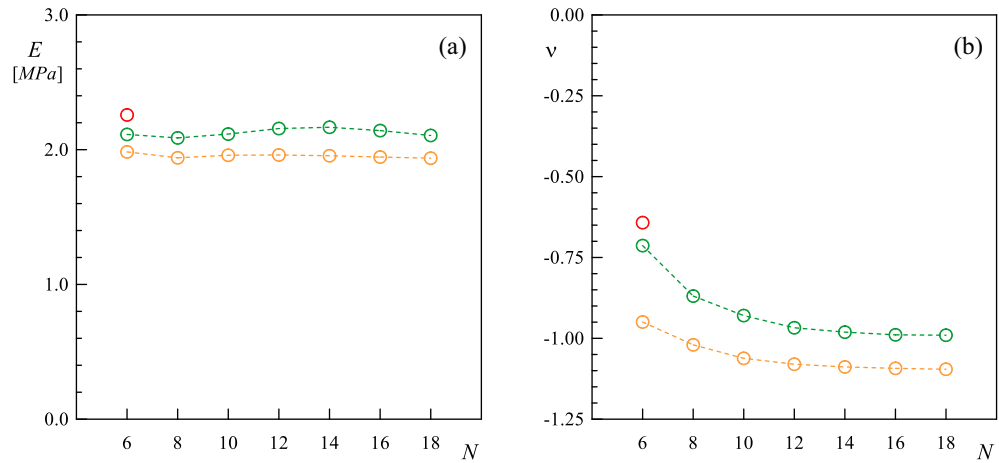

Fig. 15. Comparison between experimental results (red circle) and numerical results of the solid model (green circles) and beam lattice model (yellow circles). Global elastic properties versus cell number of the square sample (with $N = M$): (a) Young modulus E, (b) Poisson ratio ν. (For interpretation of the references to colour in this figure legend, the reader is referred to the web version of this article.)

process. The angular strain elimination is kinematically based on the independent and opposite-sign *rolling-up* mechanisms of the two component layers, reciprocally constrained at the sample boundaries. Specifically, the boundary constraints are properly designed to impose identical layer-to-layer displacements to the rings, which remain free to rotate independently.

As main macroscopic consequence of its microstructural layout, the static response of the bi-tetrachiral material – composed of collaborating non-auxetic layers – exhibits a remarkably strong auxeticity that can be quantified by negative global Poisson ratio close to −0.7 for the tested samples. Moreover, the bi-tetrachiral material is found to outperform the tetrachiral material also in terms of global Young modulus, which turns out to be nearly doubled under the same testing conditions. These experimental results have been closely confirmed by the qualitative and quantitative simulations obtainable with beam lattice formulations and finite element solid models. In this case, the simplifying mechanical assumptions affecting the beam lattice model determine only a minor underestimation of the global Young modulus and the global Poisson ratio. Finally, parametric analyses have been carried out to evaluate numerically the effects of the bi-tetrachiral sample size on the global elastic properties. The result trend has demonstrated that a minimum Poisson ratio close to −1 can actually be reached by increasing the distance between the sample boundaries providing the interlayer constraint. This systematic results tend to confirm that the strong auxetic behaviour is substantially independent of the sample size, that is, represents a characteristic property of the bi-tetrachiral material.

Acknowledgements

Compliance with ethical standards

The authors declare that they have no conflict of interest.

Appendix A. Supplementary material

Supplementary material to this article can be found online at https://doi.org/10.1016/j.matdes.2019.107883.

References

[1] N.A. Fleck, V.S. Deshpande, M.F. Ashby, Micro-architectured materials: past, present and future, Proc. R. Soc. Lond. A Math. Phys. Sci. 466 (2121) (2010) 2495–2516.
[2] T.A. Schaedler, W.B. Carter, Architected cellular materials, Annu. Rev. Mater. Res. 46 (2016) 187–210.
[3] L.R. Meza, A.J. Zelhofer, N. Clarke, A.J. Mateos, D.M. Kochmann, J.R. Greer, Resilient 3D hierarchical architected metamaterials, Proc. Natl. Acad. Sci. U. S. A. 112 (37) (2015) 11502–11507.
[4] Y.J. Chen, F. Scarpa, Y.J. Liu, J.S. Leng, Elasticity of anti-tetrachiral anisotropic lattices, Int. J. Solids Struct. 50 (6) (2013) 996–1004.
[5] K.K. Saxena, R. Das, E.P. Calius, Three decades of auxetics research — materials with negative Poisson's ratio: a review, Adv. Eng. Mater. 18 (11) (2016) 1847–1870.
[6] C.S. Ha, M.E. Plesha, R.S. Lakes, Chiral three-dimensional isotropic lattices with negative Poisson's ratio, Phys. Status Solidi B Basic Solid State Phys. 253 (7) (2016) 1243–1251.
[7] R.S. Lakes, Negative-Poisson's-ratio materials: auxetic solids, Annu. Rev. Mater. Res. 47 (2017) 63–81.
[8] K. El Nady, F. Dos Reis, J.F. Ganghoffer, Computation of the homogenized nonlinear elastic response of 2D and 3D auxetic structures based on micropolar continuum models, Compos. Struct. 170 (2017) 271–290.
[9] Y. Rahali, F. Dos Reis, J.F. Ganghoffer, Multiscale homogenization schemes for the construction of second-order grade anisotropic continuum media of architectured materials, Int. J. Multiscale Comput. Eng. 15 (1) (2017).
[10] X. Ren, R. Das, P. Tran, T.D. Ngo, Y.M. Xie, Auxetic metamaterials and structures: a review, Smart Mater. Struct. 27 (2) (2018), 023001.
[11] O. Duncan, T. Shepherd, C. Moroney, L. Foster, P. Venkatraman, K. Winwood, T. Allen, A. Alderson, Review of auxetic materials for sports applications: expanding options in comfort and protection, Appl. Sci. 8 (6) (2018) 941.
[12] N. Karathanasopoulos, F. Dos Reis, H. Reda, J.F. Ganghoffer, Computing the effective bulk and normal to shear properties of common two-dimensional architectured materials, Comput. Mater. Sci. 154 (2018) 284–294.
[13] A. Spadoni, M. Ruzzene, S. Gonella, F. Scarpa, Phononic properties of hexagonal chiral lattices, Wave Motion 46 (7) (2009) 435–450.
[14] K.F. Tee, A. Spadoni, F. Scarpa, M. Ruzzene, Wave propagation in auxetic tetrachiral honeycombs, J. Vib. Acoust. 132 (3) (2010) 031007.
[15] Y. Rahali, F. Dos Reis, J.F. Ganghoffer, Multiscale homogenization schemes for the construction of second-order grade anisotropic continuum media of architectured materials, Int. J. Multiscale Comput. Eng. 15 (1) (2017).
[16] M. Lepidi, A. Bacigalupo, Parametric design of the band structure for lattice materials, Meccanica 53 (3) (2018) 613–628.
[17] F. Vadalà, A. Bacigalupo, M. Lepidi, L. Gambarotta, Bloch wave filtering in tetrachiral materials via mechanical tuning, Compos. Struct. 201 (2018) 340–351.
[18] A. Bacigalupo, M. Lepidi, G. Gnecco, F. Vadalà, L. Gambarotta, Optimal design of the band structure for beam lattice metamaterials, Front. Mater. 6 (2019) 2.
[19] M. Ranjbar, L. Boldrin, F. Scarpa, S. Neild, S. Patsias, Vibroacoustic optimization of anti-tetrachiral and auxetic hexagonal sandwich panels with gradient geometry, Smart Mater. Struct. 25 (5) (2016), 054012.
[20] A. Bacigalupo, L. Gambarotta, Wave propagation in non-centrosymmetric beam-lattices with lumped masses: discrete and micropolar modeling, Int. J. Solids Struct. 118 (2017) 128–145.
[21] D. Tallarico, N.V. Movchan, A.B. Movchan, D.J. Colquitt, Tilted resonators in a triangular elastic lattice: chirality, Bloch waves and negative refraction, J. Mech. Phys. Solids 103 (2017) 236–256.
[22] A. Bacigalupo, M. Lepidi, Acoustic wave polarization and energy flow in periodic beam lattice materials, Int. J. Solids Struct. 147 (2018) 183–203.
[23] R. Lakes, Deformation mechanisms in negative Poisson's ratio materials: structural aspects, J. Mater. Sci. 26 (9) (1991) 2287–2292.
[24] A. Alderson, K.L. Alderson, D. Attard, K.E. Evans, R. Gatt, J.N. Grima, W. Miller, N. Ravirala, C.W. Smith, K. Zied, Elastic constants of 3-, 4-and 6-connected chiral and anti-chiral honeycombs subject to uniaxial in-plane loading, Compos. Sci. Technol. 70 (7) (2010) 1042–1048.
[25] A. Lorato, P. Innocenti, F. Scarpa, A. Alderson, K.L. Alderson, K.M. Zied, N. Ravirala, W. Miller, C.W. Smith, K.E. Evans, The transverse elastic properties of chiral honeycombs, Compos. Sci. Technol. 70 (7) (2010) 1057–1063.
[26] A. Alderson, K.L. Alderson, G. Chirima, N. Ravirala, K.M. Zied, The in-plane linear elastic constants and out-of-plane bending of 3-coordinated ligament and cylinder-ligament honeycombs, Compos. Sci. Technol. 70 (7) (2010) 1034–1041.
[27] H. Li, Y. Ma, W. Wen, W. Wu, H. Lei, D. Fang, In plane mechanical properties of tetrachiral and antitetrachiral hybrid metastructures, J. Appl. Mech. 84 (8) (2017), 081006.
[28] C. Ma, H. Lei, J. Hua, Y. Bai, J. Liang, D. Fang, Experimental and simulation investigation of the reversible bi-directional twisting response of tetra-chiral cylindrical shells, Compos. Struct. 203 (2018) 142–152.
[29] W. Wu, L. Geng, Y. Niu, D. Qi, X. Cui, D. Fang, Compression twist deformation of novel tetrachiral architected cylindrical tube inspired by towel gourd tendrils, Extreme Mech. Lett. 20 (2018) 104–111.
[30] M. Li, X. Lu, X. Zhu, X. Su, T. Wu, Research on in-plane quasi-static mechanical properties of gradient tetra-chiral hyper-structures, Adv. Eng. Mater. (2018) 1801038, https://doi.org/10.1002/adem.201801038.
[31] Y. Jiang, Y. Li, Novel 3d-printed hybrid auxetic mechanical metamaterial with chirality-induced sequential cell opening mechanisms, Adv. Eng. Mater. 20 (2) (2018), 1700744.
[32] M. Fu, F. Liu, L. Hu, A novel category of 3D chiral material with negative Poisson's ratio, Compos. Sci. Technol. 160 (2018) 111–118.
[33] W. Wu, D. Qi, H. Liao, G. Qian, L. Geng, Y. Niu, J. Liang, Deformation mechanism of innovative 3D chiral metamaterials, Sci. Rep. 8 (1) (2018) 12575.
[34] N. Guo, M.C. Leu, Additive manufacturing: technology, applications and research needs, Front. Mech. Eng. 8 (3) (2013) 215–243.
[35] Y. Jiang, Y. Li, 3D printed chiral cellular solids with amplified auxetic effects due to elevated internal rotation, Adv. Eng. Mater. 19 (2) (2017), 1600609.
[36] T. Li, Y. Chen, X. Hu, Y. Li, L. Wang, Exploiting negative Poisson's ratio to design 3D-printed composites with enhanced mechanical properties, Mater. Des. 142 (2018) 247–258.
[37] D. Chen, X. Zheng, Multi-material additive manufacturing of metamaterials with giant, tailorable negative Poisson's ratios, Sci. Rep. 8 (2018) 9139.
[38] T.A. Schaedler, W.B. Carter, Architected cellular materials, Annu. Rev. Mater. Res. 46 (2016) 187–210.
[39] J.T. Muth, P.G. Dixon, L. Woish, L.J. Gibson, J.A. Lewis, Architected cellular ceramics with tailored stiffness via direct foam writing, Proc. Natl. Acad. Sci. U. S. A. 114 (8) (2017) 1832–1837.

[40] G. Dong, Y. Tang, Y.F. Zhao, A survey of modeling of lattice structures fabricated by additive manufacturing, J. Mech. Des. 139 (10) (2017), 100906.

[41] I. Maskery, L. Sturm, A.O. Aremu, A. Panesar, C.B. Williams, C.J. Tuck, R.D. Wildman, I.A. Ashcroft, R.J.M. Hague, Insights into the mechanical properties of several triply periodic minimal surface lattice structures made by polymer additive manufacturing, Polymer 152 (2018) 62–71.

[42] A. Vyatskikh, S. Delalande, A. Kudo, X. Zhang, C.M. Portela, J.R. Greer, Additive manufacturing of 3D nano-architected metals, Nat. Commun. 9 (1) (2018) 593.

[43] Y. Sha, L. Jiani, C. Haoyu, R.O. Ritchie, X. Jun, Design and strengthening mechanisms in hierarchical architected materials processed using additive manufacturing, Int. J. Mech. Sci. 149 (2018) 150–163.

[44] K. Melde, A.G. Mark, T. Qiu, P. Fischer, Holograms for acoustics, Nature 537 (7621) (2016) 518.

[45] F. Auricchio, S. Marconi, 3D printing: clinical applications in orthopaedics and traumatology, EFORT Open Rev. 1 (5) (2016) 121–127.

[46] A.J. Capel, R.P. Rimington, M.P. Lewis, S.D. Christie, 3D printing for chemical, pharmaceutical and biological applications, Nat. Rev. Chem. 2 (2018) 422–436.

[47] E. Massoni, L. Silvestri, M. Bozzi, L. Perregrini, G. Alaimo, S. Marconi, F. Auricchio, Characterization of 3D-printed dielectric substrates with different infill for microwave applications, 2016 IEEE MTT-S IMWS-AMP, 2016.

[48] H. Cui, R. Hensleigh, D. Yao, D. Maurya, P. Kumar, M.G. Kang, S. Priya, X.R. Zheng, Three-dimensional printing of piezoelectric materials with designed anisotropy and directional response, Nat. Mater. 18 (3) (2019) 234–241.

[49] S.H. Huang, P. Liu, A. Mokasdar, L. Hou, Additive manufacturing and its societal impact: a literature review, Int. J. Adv. Manuf. Technol. 67 (5–8) (2013) 1191–1203.

[50] F. Auricchio, A. Greco, G. Alaimo, V. Giacometti, S. Marconi, V. Mauri, 3D printing technology for buildings accessibility: the tactile map for MTE museum in Pavia, J. Civ. Eng. Archit. 11 (2017) 736–747.

[51] A. Bacigalupo, L. Gambarotta, Homogenization of periodic hexa-and tetrachiral cellular solids, Compos. Struct. 116 (2014) 461–476.

[52] Y. Chen, X.N. Liu, G.K. Hu, Q.P. Sun, Q.S. Zheng, Micropolar continuum modelling of bi-dimensional tetrachiral lattices, Proc. R. Soc. Lond. A Math. Phys. Sci. 470 (2165) (2014), 20130734.

[53] L. Cabras, M. Brun, Auxetic two-dimensional lattices with Poisson's ratio arbitrarily close to −1, Proc. R. Soc. Lond. A Math. Phys. Sci. 470 (2014) (20140538-20140538).

[54] G. Alaimo, S. Marconi, L. Costato, F. Auricchio, Influence of meso-structure and chemical composition on FDM 3D-printed parts, Compos. Part B 113 (2017) 371–380.